IEEE Access
Multidisciplinary | Rapid Review | Open Access Journal

Received 17 July 2023, accepted 17 August 2023, date of publication 1 September 2023, date of current version 8 September 2023.

Digital Object Identifier 10.1109/ACCESS.2023.3311352

RESEARCH ARTICLE

Design and Control of an Individualized Hip Exoskeleton Capable of Gait Phase Synchronized Flexion and Extension Torque Assistance

SANDER DE GROOF[1], YANG ZHANG[2], LAURENT PEYRODIE[3], AND LUC LABEY[1]
[1]Department of Mechanical Engineering, Biomechanics Division, KU Leuven, 2440 Geel, Belgium
[2]Core Laboratories Productions, Flanders Make, 8500 Kortrijk, Belgium
[3]Department of Smart System and Energy, HEI-JUNIA, 59000 Lille, France

Corresponding author: Sander De Groof (sander.degroof@kuleuven.be)

This work was supported by the Interreg 2 Seas Program 2014–2020 through the European Regional Development Fund (M.O.T.I.O.N Project) under Contract 2S05-038.

This work involved human subjects or animals in its research. The authors confirm that all human/animal subject research procedures and protocols are exempt from review board approval.

ABSTRACT Assistive single-joint lower-limb exoskeletons have shown potential clinical benefits in patients with gait deficiencies. Torque-controlled exoskeletons, unlike position-controlled exoskeletons, do not restrict voluntary movements, allowing for safer interaction with the user. A torque-controlled hip flexion/extension exoskeleton intended for individuals with cerebral palsy is presented in this paper. The overarching research objective is to mitigate hip extension deficit and excessive hip flexion observed in crouch gait and apparent equinus gait patterns, which may be achieved by providing an extension torque during the stance phase. We expound on the design of an exoskeleton capable of performing this task, including a detailed discussion of the design, torque control, and benchmarking of its actuators. The device features series elastic actuators with a low output impedance and individualized orthotics designed using algorithmic 3D modeling and manufactured using additive manufacturing technologies. The exoskeleton's mechanical structure, orthotics, control, user interface, and safety functions are presented. A performance evaluation was conducted through a trial on an unimpaired participant (174 cm, 74.5 kg). Up to 35 Nm of extension torque during stance could be achieved during walking on a treadmill with a stride time of 1.2 s. The participant was asked to simulate a crouched gait and experienced a lifting sensation at approximately 16 Nm of extension torque during stance, making it difficult to maintain the crouch.

INDEX TERMS Actuators, exoskeletons, rehabilitation robotics, torque control.

I. INTRODUCTION

Cerebral Palsy (CP) is a neurological condition caused by a lesion in the developing brain of a child, permanently affecting motor function [1]. CP is estimated to occur in 1.5 to 3 in 1000 live births in Europe [2]. Although CP causes motor function impairment, approximately 70% of CP children are ambulatory [3]. According to Beckung et al. [4], 50% of CP children can walk without assistance and a further 16% need walking aids. The level of motor impairment varies among CP patients, ranging from mild to severe. The Gross Motor Function Classification System (GMFCS) is a five-tier scale (I, II,... V) [5] used to classify CP patients [6]. CP children classified as GMFCS I (walking without limitations), GMFCS II (walking with limitations), and GMFCS III (walks using a hand-held mobility device) could benefit from assistive robotic technologies allowing voluntary movements, such as torque- or force-controlled exoskeletons.

Children with CP can develop a pathological gait because of spasticity, muscle weakness, and reduced neuromuscular control [5]. The motion of multiple joints can deviate from typical gait. Clinicians classify the gait into six patterns [3]:

The associate editor coordinating the review of this manuscript and approving it for publication was Zhuang Xu.

(1) genu recurvatum, (2) drop foot, (3) true equinus, (4) jump gait, (5) apparent equinus, and (6) crouch gait. Apparent equinus and crouch gait feature excessive hip and knee flexion during stance. Hip extension deficit and continuous excessive hip flexion are observed significantly more frequently in GMFCS II and GMFCS III, with respect to GMFCS I [1].

Commercially available lower-limb exoskeletons have been used for gait training of CP patients, such as the Hybrid Assistive Limb (HAL®) by Cyberdyne Inc, which has been tested extensively on CP patients [7], [8], [9], [10]. The HAL contains four actuated degrees of freedom (DOFs), located at the hip and knee to assist sagittal plane motions. A pediatric version of the HAL (2SHAL) was recently developed [7]. Significant improvements were demonstrated in spatiotemporal gait parameters such as cadence, walking speed, single-leg support phase, and hip angle during the swing phase [8]. However, these exoskeletons are usually position controlled, which imposes the motion, restricts voluntary movements, and may even result in injury, especially in CP, because of muscle contractures and spasticity [11].

To overcome these position control limitations, researchers have been developing compliant exoskeletons. Marsi Bionics, a spin-off of the Centro de Automática y Robótica (CAR), a joint center of the Universidad Politécnica de Madrid (UPM), has developed the Atlas Pediatric Exo 2030, a pediatric active Trunk-Hip-Knee-Ankle-Foot Orthosis (THKAFO) [12]. It has six actuated DOFs, 3 per leg: hip and knee flexion/extension and ankle dorsiflexion/plantarflexion. The actuators at the knee and hip are variable stiffness actuators (VSA). The passive compliance of the knee and ankle joint can be adjusted using a second motor during operation. The hip joint is a regular rotary series elastic actuator (SEA) with fixed compliance. Furthermore, the knee joint features a locking mechanism, which can make this joint into a passive mechanism on demand [13]. Other researchers have designed exoskeletons that interact with a single joint, e.g., the ankle joint [14], [15], the knee joint [16] and the hip joint [17].

Giovacchini et al. [18] designed an active pelvis orthosis (APO), a hip flexion and extension exoskeleton intended for gait assistance in the elderly. The authors showed that torque-controlled SEAs can be successfully integrated into a hip exoskeleton and can provide gait-synchronized torque assistance. Gait synchronization was achieved through the use of adaptive oscillators. The authors noted the need for sufficiently stable orthotics. Recent research on powered ankle-foot orthotics confirmed that individualized orthotics reduce relative motion between the body and the orthotics and increase power transmission efficiency [19].

Kang et al. [20] designed a SEA-based bilateral hip exoskeleton and investigated the effect of properly timed assistive torques on the metabolic cost of walking in unimpaired participants. A trapezoidal flexion torque setpoint during the swing phase and a trapezoidal extension torque setpoint during the stance phase were provided. Four assistive torque magnitudes, relative to the biological peak joint torques, were tested: 0%, 13%, 26%, and 40%. A U-shaped trend was observed between assistance magnitude and metabolic cost. Moreover, when optimized, a 6% average reduction in metabolic cost was observed, showing that a simple assistive torque scheme, when timed and scaled appropriately, can aid humans in expending less energy during walking. Gait synchronization was achieved by recording the time between heel strikes, using force-sensitive resistors (FSRs), and employing the moving average of the five most recent stride times to extrapolate the progression of the current gait cycle. This method introduces a delay that can lead to improperly timed assistance in case of inconsistent walking speed.

Recently, Bishe et al. [17] designed a hip flexion and extension exoskeleton with a user-adaptive high-level control strategy. The authors performed a feasibility study on a single adult with CP. The study showed reduced metabolic cost (15%), hip flexion (14°), hip flexor muscle activity (23%), and extensor muscle activity (46%). FSRs incorporated into the shoe soles were used for gait synchronization and hip torque estimation. These sensors are known to have low durability [21].

Our research aims to investigate the feasibility of a torque-controlled hip flexion/extension exoskeleton to achieve clinical benefits for patients with motor function impairments such as CP. We hypothesize that providing extension torque during one or more stance phases (loading response, midstance, terminal stance) could reduce hip extension deficit and continuous excessive hip flexion in crouch gait and apparent equinus CP gait patterns.

Our aim with this work was to develop a hip exoskeleton that satisfies these requirements: (1) The actuators must be capable of delivering sufficient torque. (2) Torque control must possess adequate bandwidth and tracking precision. (3) The orthotics must transmit torque to the body without causing any discomfort. (4) Hip abduction and adduction should be feasible without causing excessive relative motion and pressure between the orthotics and the body. (5) The detection of gait phases must be dependable and real-time, without any unnecessary delays. A recent review of mechanical design principles of compliant exoskeletons reveals a lack of detailed technical information regarding these devices [22]. Therefore, a comprehensive description of our device is given.

The structure of this paper is as follows. First, the system components are presented at a high level of abstraction. Second, the design, torque control, and benchmarking sections discuss the actuators in detail. The benchmark comprises the controlled system's time and frequency domain response and an output impedance characterization. Third, the exoskeleton's mechanical structure, orthotics, and abduction/adduction mechanism are presented. Fourth, the exoskeleton's control, user interface, operation, and safety are discussed. Fifth, a trial on an unimpaired participant is presented, wherein the performance of the transparent mode, the

maximum torque capability, and the effect of extension torque during stance on simulated crouch gait are investigated. Finally, the main findings are summarized, and suggestions for future work and improvements to the exoskeleton are given.

II. MOTION HIP EXOSKELETON

A. SYSTEM DESCRIPTION

The system architecture, shown in Fig. 1, consisted of on-board and off-board components, as is indicated by the dashed vertical line. The right leg components were omitted because of symmetry. The control system consisted of a laptop running MATLAB (MathWorks Inc.) and a user interface designed in MATLAB App Designer. The real-time software was designed using Simulink Real-time, and the control tasks were executed at 1 kHz. The code was compiled to run on a "Unit" Real-time target machine (Speedgoat GmbH, Switzerland). The target was connected to the host PC with the host link port, and the ETH1 port was configured as EtherCAT master, which handled all I/O on the exoskeleton. The EtherCAT network consists of a remote I/O node (EK1100 bus coupler, EL5042 2x BiSS-C encoder inputs, EL3102 2x -10/+10V analog inputs, Beckhoff Automation GmbH & Co. KG, Germany), two motor controllers (EPOS4 Compact 50/15 Ethercat" positioning controller, article No. 605299, maxon motor AG, Switzerland) and two IMUs (Mti-1, Xsens Technologies BV, Netherlands, EtherCAT slave board by Gable systems BVBA, Netherlands). The on-board electronics also contain a custom PCB with the following functions: 3 × 2 RJ45 connectors for EtherCAT patching, a 24V-5V DC-DC converter (TSR 1-2450, TRACO Power) to power the IMUs, voltage sensing using a voltage divider, and current sensing utilizing a shunt resistor and an amplifier (INA191, Texas instruments Incorporated). A safety circuit was implemented in hardware using the Safe-Torque-Off (STO) inputs on the motor controllers. An enabling switch (XY2AU1, Schneider Electric), which has two contacts that break when the operator releases or hard-presses the grip button, was connected to a safety relay (Pnoz s4+s7, Pilz GmbH & Co. KG, Germany). Each motor controller has 2 STO inputs and was wired to two safety relay contacts. The motor controllers were powered by an AC/DC 24V 20A power supply (TRIO-PS/1AC/24DC/20, article No. 2866381, Phoenix Contact). To prevent voltage spikes when energy is fed back to the power supply, a shunt regulator set to 27 VDC was placed in parallel with the power supply as an off-board component (DSR50/5, article No. 309687, maxon motor AG, Switzerland). A second AC/DC 24V power supply was used to power the remote I/O to protect it from voltage spikes. The SEA is described further in section II-B.

B. ACTUATOR DESIGN

A novel SEA was designed and is presented in Fig. 2. In previous work [23], we presented the selection of a feasible motor and reduction ratio combination (based on [24])

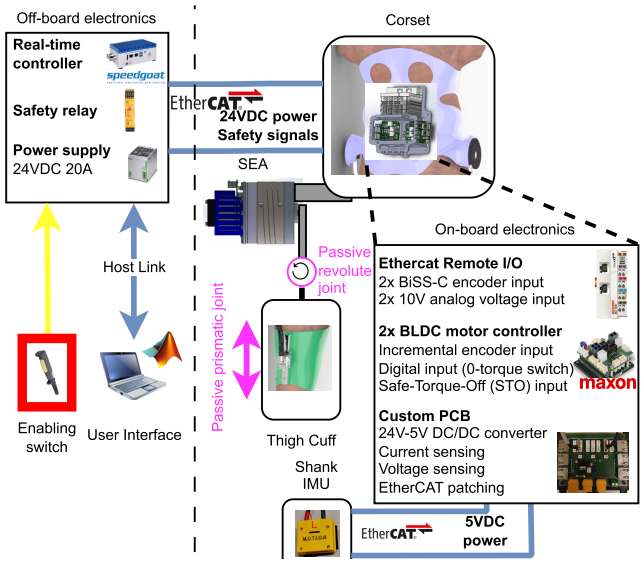

FIGURE 1. Exoskeleton system diagram.

and the spring stiffness, using numerical methods and gait data, which reduced the risk of undersizing the actuator [25]. The SEA consists of the following components: (Fig. 2, A) a BLDC motor (EC60 flat-150W-24V, article No. 625858, maxon motor AG, Switzerland) with a built-in incremental encoder (Encoder MILE, 4096 counts per turn, 2-channel, with line driver, article No. 651168), (Fig. 2, B) a harmonic drive (HD) (SHD20-80-2SH, Harmonic Drive SE, Germany), requiring specialized grease (SK-1A), and with a reduction ratio of 81, when the flex spline (FS) is the velocity reference, (Fig. 2, C) deep groove ball bearings of size 45 mm × 58 mm × 7 mm (6809ZZ, NSK Ltd., Japan), (Fig. 2, D) a magnetic absolute single-turn encoder (AKSIM-2, Renishaw PLC, England) consisting of a magnetic ring (MRA053BC030DSE00) and a read head (MB053DCC20BENT00), and (Fig. 2, E) a slotted optical switch to signal zero-torque (EE-SX3162-P2, Omron Corporation, Japan). Furthermore, the SEA contains a custom machined spring (Fig. 2, F). The actuator's mechanical connection to the exoskeleton's corset is referred to as the output hub (Fig. 2, G), and the connection to the lever arm that connects to the thigh cuff is referred to as the output shaft (Fig. 2, H). Fig. 3 shows the four rigid bodies of the SEA.

- Body 1 is the rotor of the BLDC motor, connected to the wave generator (WG) of the HD.
- Body 2 is the stator of the BLDC motor, connected to the FS of the HD, and the spring.
- Body 3 is the HD's circular spline (CS), connected to the actuator's output shaft.
- Body 4 is the output hub of the actuator, which is connected to the other side of the spring.

The positions and velocities of rigid bodies 1, 2, and 3 are related through the HD reduction ratio, N, by equation (1).

$$N = \frac{\theta_1 - \theta_2}{\theta_3 - \theta_2} = 81. \tag{1}$$

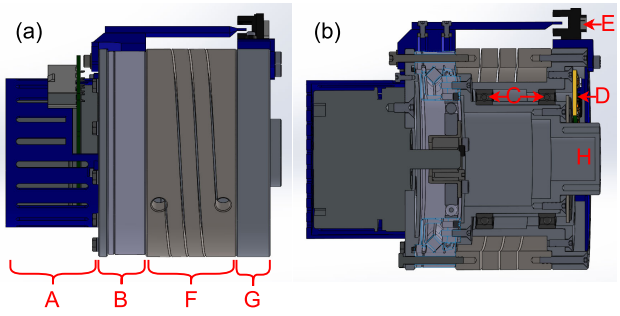

FIGURE 2. Series elastic actuator component overview: (a) side view and (b) section view. Components: BLDC motor and encoder (A), Harmonic Drive (B), ball bearings (C), output encoder (D), optical slotted switch (E), series spring (F), output hub (G), and output shaft (H).

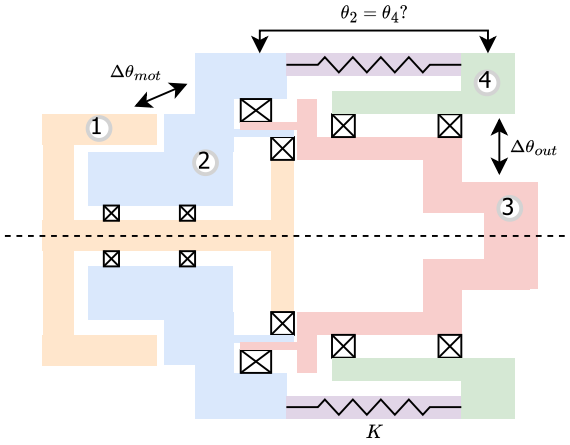

FIGURE 3. Series elastic actuator body diagram. The rigid bodies are numbered 1 through 4.

The angular position of body i about the actuator axis, relative to an arbitrary fixed reference, is expressed as θ_i, and when all angular positions are zero, the spring is unloaded ($\theta_2 = \theta_4$).

An essential physical quantity of an actuator is the apparent moment of inertia, which should be minimized for a fast dynamic response. For stiff actuators, the moment of inertia of the motor's rotor must be multiplied by N^2. However, in our SEA in locked-output configuration, body 2 rotates in the opposite direction of body 1, resulting in an apparent moment of inertia I_{eq} at the output given by (2), wherein I_i is the moment of inertia of body i (as defined in Fig. 3) about the actuator axis.

$$I_{eq} = (N-1)^2 I_1 + I_2. \tag{2}$$

Using this counter-rotating setup, a reduction of the apparent moment of inertia relative to a stiff actuator can be attained if: $I_2/I_1 < 2N - 1$. The moments of inertia of the bodies about the rotation axis were estimated using CAD software (SolidWorks 2020), using the approximate geometry and material density of the parts that make up these bodies. In the case of this SEA, the apparent moment of inertia was reduced by 2.3% relative to a stiff actuator.

Another benefit of this setup is the possible lowering of the motor torque feed-through to the net output torque, i.e., the sum of the torques at the output hub and output shaft, during the transient response. The feed-through can be eliminated by tailoring the moments of inertia of bodies 1 and 2 to ensure the net angular momentum of the internal actuator components remains zero in the locked-output configuration if: $I_2/I_1 = N - 1$.

C. ACTUATOR TORQUE CONTROL

Torque sensing is a prerequisite for closed-loop torque control. Since a SEA includes an elastic element by design, the torque can be calculated by measuring the deflection of this element and using the identified spring characteristic. Two relative angular positions are measured using the motor encoder ($\Delta\theta_{mot}$) and the output encoder ($\Delta\theta_{out}$). The motor encoder is an incremental encoder and measures the rotor (body 1) position of the BLDC motor relative to the stator (body 2). This measurement can be zeroed at an arbitrary position.

$$\Delta\theta_{mot} = \theta_1 - \theta_2 \tag{3}$$

The output encoder is an absolute, single-turn encoder and measures the position of the actuator's output shaft (body 3) relative to the output hub (body 4). The reference position $\theta_{out,ref}$ can be arbitrarily chosen.

$$\Delta\theta_{out} = \theta_3 - \theta_4 = \theta_{out} - \theta_{out,ref} \tag{4}$$

For convenience in torque calculation, the motor encoder is zeroed while the spring is unloaded. The absolute encoder measurement in this state must be saved as the reference position, $\theta_{out,ref}$, in a procedure we named zero-torque homing (ZTH). The unloaded spring state is detected using the optical slotted switch, which signals if ZTH is allowed. The relative output position is determined by subtracting the reference from the measured position, using (4). The spring is inserted between bodies 2 and 4. The relationship between the spring torque τ and spring deflection φ is nearly linear and is characterized by the spring rate K, which was experimentally identified in Section II-D. The spring torque is readily calculated using (5).

$$\tau = K\varphi = K(\theta_4 - \theta_2) \tag{5}$$

A formula expressing the spring deflection φ as a function of the encoder measurements is needed. Inserting $\theta_3 - \theta_3$ and (1) into (5) and rearranging yields:

$$\varphi = \theta_3 - \theta_2 - (\theta_3 - \theta_4) = \Delta\theta_{mot}/N - \Delta\theta_{out} \tag{6}$$

The HD introduces a 1/60° backlash. Accounting for this backlash and the encoder resolutions (motor: 12 bit, output: 20 bit), the error interval of φ is estimated to be: $\sqrt{(2\pi/(N2^{12}))^2 + (2\pi/2^{20})^2 + ((\pi/180)(1/60))^2} = 2.92 \cdot 10^{-4}$rad. The backlash dominates the error because it is approximately 15 times larger than the next largest error on $\Delta\theta_{mot}$.

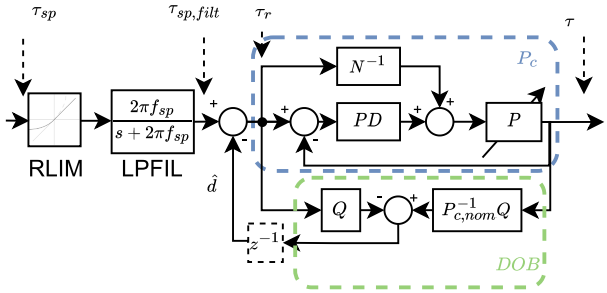

FIGURE 4. Torque controller block diagram.

Exoskeletons have time-varying load-side dynamics and are subject to unknown disturbances of a human interacting with the device. Various controller architectures have been used for closed-loop torque control of SEAs [26]. A frequently used robust control tool is the disturbance observer (DOB), which rejects disturbances and handles model parameter uncertainty by subtracting an estimated lumped disturbance $\hat{d}$ from the system input [27]. The selected low-level torque control architecture for our SEA, shown in Fig. 4, consists of a PD compensator with feedforward, and a DOB on the outer loop. Paine et al. proposed this controller for the decentralized torque control of SEAs in the NASA-JSC Valkyrie Humanoid Robot [28], [29]. The nominal controlled plant, $P_{c,nom}$, contains the SEA plant (P) in the locked-output configuration P_{nom}, in which the SEA can be approximated as a second-order mass-spring-damper system given by (7).

$$P_{nom}(s) = \frac{K\,N}{I\,s^2 + B\,s + K} \tag{7}$$

The formula for the PD compensator is denoted in (8).

$$\mathrm{PD}(s) = k_p + \frac{F_d\,k_d\,s}{F_d + s} \tag{8}$$

The derivative term is first-order lowpass filtered, with a cutoff pulsatance of F_d, to attenuate high-frequency noise. The solution of the $P_{c,nom}$ block diagram is denoted in (9).

$$P_{c,nom}(s) = \frac{K + K\,N\left(k_p + \frac{F_d\,k_d\,s}{F_d+s}\right)}{K\,N\left(k_p + \frac{F_d\,k_d\,s}{F_d+s}\right) + I\,s^2 + B\,s + K} \tag{9}$$

Equation (10) denotes the transfer function of a second-order Butterworth filter, with cutoff pulsatance F_b.

$$Q(s) = \frac{{F_b}^2}{{F_b}^2 + \sqrt{2}\,F_b\,s + s^2} \tag{10}$$

Inverting (9) and performing multiplication with (10) yields the DOB transfer function. In the theoretical analysis by Paine, the lowpass filter on the derivative term was omitted, and the proportional gain (k_p) and derivative gain (k_d) were determined by placing the poles of the resulting closed-loop, second-order system. All systems were considered linear time-invariant, and nonlinear effects in real systems, such as motor saturation and transport delay, were ignored in this analysis. (Recently, Lin et al. [30] have developed a controller that models some nonlinear effects, such as the gravity of a load-side pendulum and Coulomb friction, by estimating multiple model parameters, including the disturbance.) Section II-D discusses the issues attributed to nonlinearity and the added setpoint smoothing to mitigate the adverse effects. The formulas for gain setting [29], reliant on pole placement, did not produce a satisfactory response in our system. The gains were tuned by modeling the system in Simulink using both continuous and discrete-time blocks (hybrid model). The autotune feature of the Simulink PID block was then employed to find good values for k_p and k_d. The used controller parameters are denoted in Table 1.

TABLE 1. Used controller parameters.

Parameter	Value	Unit
EtherCAT Bus		
Update rate	1000	Hz
Transport delay	5	ms
EPOS4 Motor Current Controller		
Proportional gain	1250	mV/A
Integral gain	2200	A·ms
Peak current	15	A
Continuous current	10	A
Torque Controller Gains and Filter Constants		
k_p: Proportional gain	0.089	/
k_d: Derivative gain	0.0041	s
f_d: Derivative term lowpass filter	50	Hz
f_b: Lowpass Butterworth filter Q	10	Hz
k_{ff}: Feedforward gain ($= N^{-1}$)	0.0123	/
Setpoint smoothing		
fsp: Setpoint lowpass filter	10	Hz
rlim: Setpoint rate limiting	300	Nm/s

Laplace transform methods are the most prevalent way of designing continuous-time controllers for continuous-time plants. A controller designed this way must be discretized for execution on a digital computer. A discrete-time equivalent that behaves similarly to the continuous-time system at the sample instances must be constructed. The control engineer has several options to perform this discretization. For example, the hold logic of the D/A converter can be accounted for using the step invariant method (zero-order hold D/A logic) or the ramp invariant method (first-order hold D/A logic). Other methods approximate the differentiation by substituting the Laplace variable s with a rational function of z, such as the forward difference, backward difference, and Tustin method. Recently, other s-to-z domain mappings that ameliorate oscillations due to sudden input changes, sudden disturbances, and non-zero initial values are being researched [31]. The Tustin method provides a good frequency response match and retains stability between the continuous and discrete-time domains, although frequency warping occurs [32]. These discretization methods differ in mathematical complexity. The step invariant and impulse invariant methods require partial fraction expansion and calculation or lookup of inverse Laplace transforms and Z-transforms. Although there is a MATLAB function for these discretization methods, the *c2d* function, the Speedgoat real-time target does not support it.

This hinders tuning efforts because the DOB needs to be re-discretized when the controller gains are changed. A symbolic form of the discrete-time transfer function is the most convenient. The Tustin method involves a substitution of the Laplace variable s by $s' = (2/T)\cdot(z-1)/(z+1)$. This substitution was performed on all system components that run on the real-time controller: PD(s), $Q(s)$ and $P_{c,nom}^{-1}(s)Q(s)$, using a sample time (T) of 0.001 s. The resulting discrete-time transfer functions are rational, and the numerator and denominator can be grouped according to the powers of z, yielding a set of coefficients expressed as functions of the system parameters of the continuous-time system. To avoid error-prone manual calculations, symbolic math software (e.g., MATLAB Symbolic Math Toolbox) is recommended for this step. The resulting transfer functions' numerator and denominator polynomial coefficients are recalculated in real-time and fed into a Simulink *discrete tranfer fcn* block. Alternatively, the functions can be transformed into executable difference equations, for implementation in other programming languages, by rewriting the transfer functions in terms of z^n with $n < 0$ and using Z-transform pair $z^n X(z) \leftrightarrow x(k+n)$. It should be noted that converting $Q(s)$ to the discrete domain, $Q(z)$, using the Tustin method, makes the transfer function direct feed-through and introduces an algebraic loop that was eliminated by adding a unit delay block, z^{-1}.

D. ACTUATOR BENCHMARK

This section elaborates on the performance benchmarking experiments performed on the actuators. The bode plots presented in this section were generated from experimental data using the MATLAB Signal Processing toolbox function *tfestimate*. The signals were windowed using hamming windows with 50% overlap, and the window length varied across experiments, depending on the lowest frequency contained in the chirp excitation signal.

The spring stiffness was the first parameter to be identified. A test setup (Fig. 5) was built, featuring the SEA (Fig. 5, A), a 200 mm lever arm (Fig. 5, B), and an S-beam loadcell (Fig. 5, C) rated for 250 N. The loadcell (SSMF, Interface, Inc., United States) was connected to the EtherCAT network (EL3356-0010, Beckhoff Automation GmbH & Co. KG, Germany). A maximum torque (τ_{max}) of approximately 20 Nm was targeted for this experiment because of the continuous torque limit of the motor. A complete loading cycle, $+\tau_{max}$ to $-\tau_{max}$ and back to $+\tau_{max}$, was performed to capture the hysteresis. A positive deflection causes the helix to wind up. A negative deflection causes the helix to unwind. The spring deflection φ was calculated using the built-in encoder measurements. The torque τ was measured by multiplying the load cell force by the lever arm's length (0.2 m). Consistent fit results were obtained across iterations, with R^2 values greater than 0.9995, and a value of 200 Nm/rad was adopted. Hereafter, all torque measurements are calculated by multiplying the measured spring deflection with this identified spring stiffness. Thus, they are subject to inaccuracies caused by the encoder system, backlash in the HD, and hysteresis.

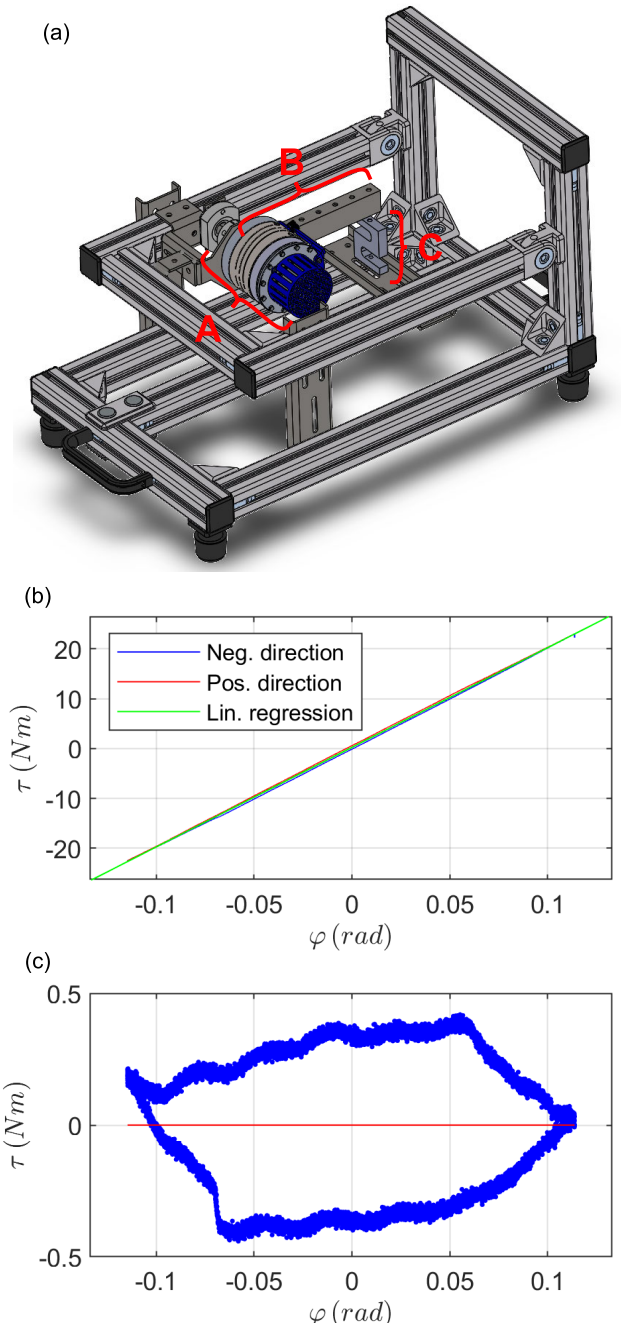

FIGURE 5. Spring stiffness identification (a) test setup, (b) measurements, and (c) residuals of the fit.

Subsequent experiments were carried out using the mechanical output configurations, shown in Fig. 6. The locked-output configuration was used to identify an approximate second-order system necessary for the DOB and simulation purposes. A logarithmic chirp signal with a frequency ranging from 1 Hz to 500 Hz and with an amplitude of 0.15 Nm was commanded to the motor. Fig. 10 shows the bode plot of this experiment. By fitting the data to (7) using the MATLAB System Identification Toolbox and setting the

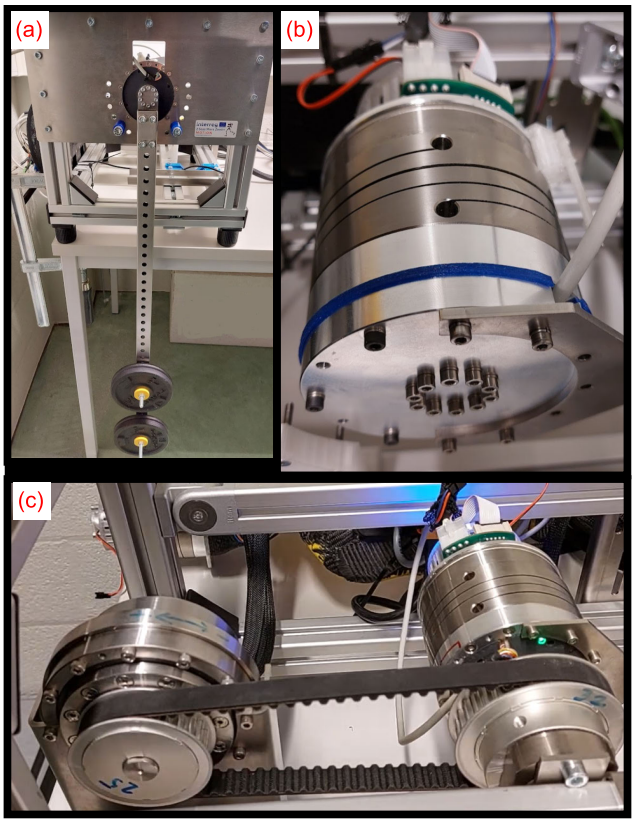

FIGURE 6. Mechanical output configurations: (a) pendulum, (b) locked-output, and (c) servo.

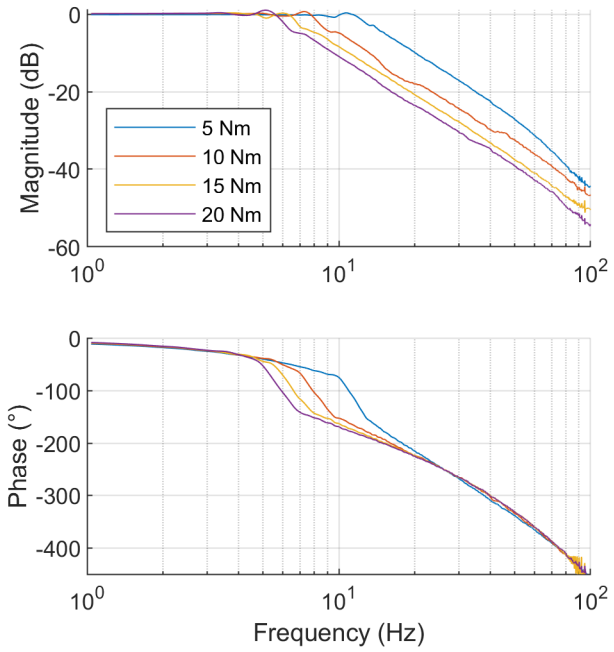

FIGURE 7. Bode plot of spring torque setpoint to measured spring torque at various chirp amplitudes.

transport delay to the measured value of 5 ms, these numerical results were obtained: $N = 73.51$, $K = 200\,\mathrm{Nm/rad}$, $B = 6.982\,\mathrm{Nm \cdot s/rad}$, $I = 0.5818\,\mathrm{kg \cdot m^2}$. The normalized rms error (NRMSE) based goodness-of-fit was 80%. The RL gain is less than the reduction ratio of the gearbox due to losses in the HD. For control purposes, we used the theoretical value: $N = 81$. Frequency response experiments were performed in the locked-output configuration on the controlled SEA system P_c without DOB, and the excitation was applied to τ_r. Step response experiments were performed on P_c with DOB. Nonlinearities such as motor saturation and transport delay in the control loop produce resonance in the closed-loop response, as well as excessive overshoot and ringing in the step response, relatively increasing with step size. These detrimental effects were attenuated by first-order lowpass filtering (LPFIL) and rate limiting (RLIM), respectively. The controlled bandwidth of the SEA in locked output was determined using a 1-100 Hz logarithmic chirp torque setpoint with 5 Nm, 10 Nm, 15 Nm, and 20 Nm amplitudes. Step response experiments with step sizes 5 Nm and 15 Nm were performed 20 times in 4 conditions: (1) regular step, (2) RLIM, (3) LPFIL, and (4) both RLIM and LPFIL, which represents the final implemented smoothing of the setpoint. A paired t-test with unequal variance and significance factor of 5% was used to test for changes in overshoot, rise time, and 2% settle time. The bandwidth at 5 Nm, 10 Nm, 15 Nm, and 20 Nm was found to be 13.8 Hz, 8.5 Hz, 7.0 Hz, and 6.2 Hz, respectively (Fig. 7). The step response experiments (Fig. 8) showed significant ($p<0.05$) improvements in response metrics by using setpoint smoothing, consisting of 300 Nm/s rate limiting to prevent saturation and 10 Hz lowpass filtering to attenuate the closed-loop resonance. With 5 Nm steps, overshoot decreased from 47.5% ± 1.07% (mean±s.d.) to 20.7% ± 0.78%. The rise time increased from 14.9 ms ± 0.3 ms to 16.1 ms ± 0.3 ms, and the 2% settle time increased from 151 ms ± 0.8 ms to 163 ms ± 10 ms. With 15 Nm steps, the overshoot decreased dramatically, from 91.6% ± 1.1% to 1.80% ± 0.13%. While the rate-limiting (ramp function) causes an evident increase in rise time, 25.6 ms ± 0.5 ms to 37.9 ms ± 0.2 ms, the 2% settle time is decreased from 411 ms ± 20 ms to 103 ms ± 5 ms, resulting in the system reaching steady-state faster, without ringing.

To ensure stability when the output is not locked, i.e., when the actuator interacts with a human during gait, the controller should be verified in the worst-case condition, i.e., minimal output moment of inertia. The exoskeleton user's minimum leg moment of inertia about the hip flexion/extension axis was estimated in 60° knee flexion, using regression formulas for inertial parameters of human body parts by Patel et al. [5]. A pendulum with evenly spaced holes and configurable moment of inertia was configured with 1 kg weight. The position and amount of weights that produced a moment of inertia that closely matched the approximated leg inertia were determined by an optimization.

In the experiment shown in Fig. 9, the spring torque setpoint is 0 Nm, and the 2.2 $\mathrm{kg \cdot m^2}$ pendulum is moved vigorously by hand during the first 3 seconds of this plot.

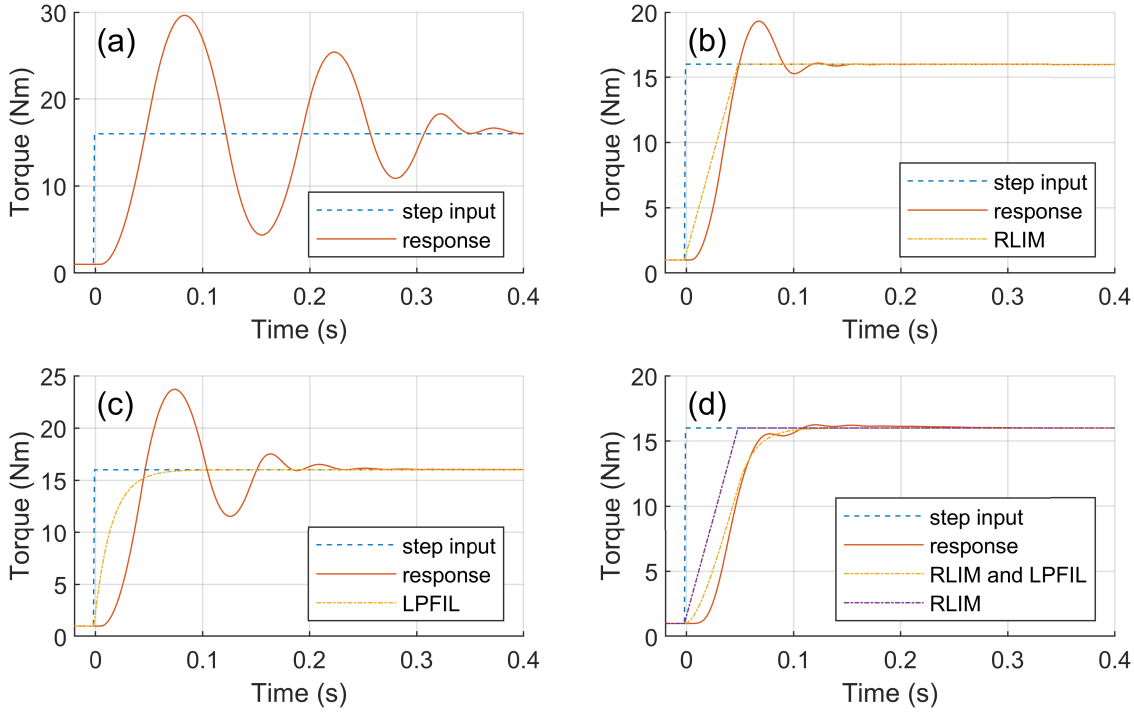

FIGURE 8. Step response to a 15 Nm step, with (a) no smoothing, (b) rate limiting 300Nm/s, (c) lowpass filtering 10 Hz, (d) rate limiting and lowpass filtering.

The peak and rms errors are approximately 0.57 Nm and 0.25 Nm, respectively. The system remained stable with the cut-off frequency of the lowpass filter Q set to 10 Hz.

The output impedance of the SEA is a useful measure to quantify the resistance felt by the human interacting with the exoskeleton. Mechanical impedance Z is defined as the ratio between force/torque (F,M) through a mechanical system and the (rotational) velocity difference (ω,v) across the system. In Laplace form, for rotational mechanical systems, the equation for impedance is $M(s) = Z(s)\omega(s)$. Giovacchini et al. characterized the output impedance of their APO by manually applying a disturbance to the output position in a quasi-sinusoidal way [18]. This leads to an ill-defined frequency spectrum, making the estimated frequency response less accurate. In our test setup, the output impedance was characterized by using a servo (Fig. 6c) to apply three logarithmic chirp velocity signals with upper frequency bounds of 5, 7, and 10 Hz and velocity amplitudes of 1.2337, 1, and 0.5 rad/s, respectively, to the output shaft of the SEA, which was set to track a constant torque of 5 Nm to prevent torque reversal and thus backlash in the servo-to-SEA coupling. The lowering of the velocity amplitude at higher frequencies prevented saturation of the motor and assured good tracking of the velocity setpoint. Fig. 11 shows the result of the experiments. The amplification between the measured impedance and the impedance of an ideal 200 Nm/rad spring, which approximates the incorporated spring, serves as a performance metric of the SEA and its control system. Table 2 shows some numerical values from the bode plot.

TABLE 2. Output impedance numerical results.

Frequency (Hz)	Impedance (Nm·s/rad)	Equivalent stiffness (Nm/rad)	Amplification w.r.t. 200Nm/rad spring (dB)
0.55	0.0522	0.180	-61
3.2	0.6116	12.4	-24
5.0	1.0933	34.4	-15
7.0	1.7497	76.5	-8.3
9.9	2.4700	153	-2.3

Where the plots of experiments with different velocity amplitudes overlap, the experiment with the highest amplitude is included in the table. The output impedance was equivalent to a 12.4 Nm/rad spring at 3.2Hz (-24 dB). At 10 Hz, the equivalent stiffness was 153 Nm/rad (-2.3dB).

E. ORTHOTICS AND MECHANICAL STRUCTURE

Researchers at Mobilab&Care designed the orthotics and mechanical structure of the hip exoskeleton. This section provides a summary of the design principles and materials used. A more detailed description may be provided in future publications by researchers at Mobilab&Care.

The exoskeleton was designed using Rhinoceros 3D modeling software and the Grasshopper algorithmic 3D modeling extension. Starting from a detailed 3D scanned mesh (Artec Leo 3D scanner) of the trial participant, the inside surfaces of the orthotics were determined. The anatomical positions of the hip joint and the femur axis were algorithmically estimated. The mechanical connections for the actuators were

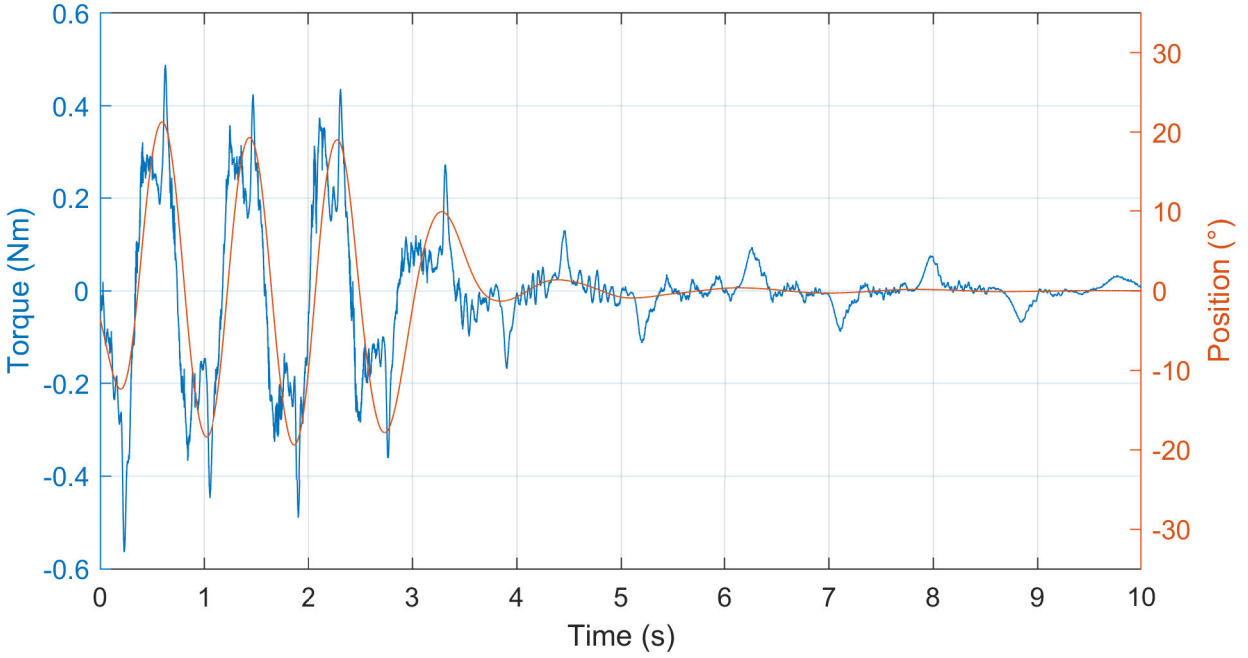

FIGURE 9. Pendulum experiment with 0 Nm setpoint, measured spring torque (blue), and output angle (red). During the first 3 seconds, the pendulum is moved by hand, after which it is held motionless.

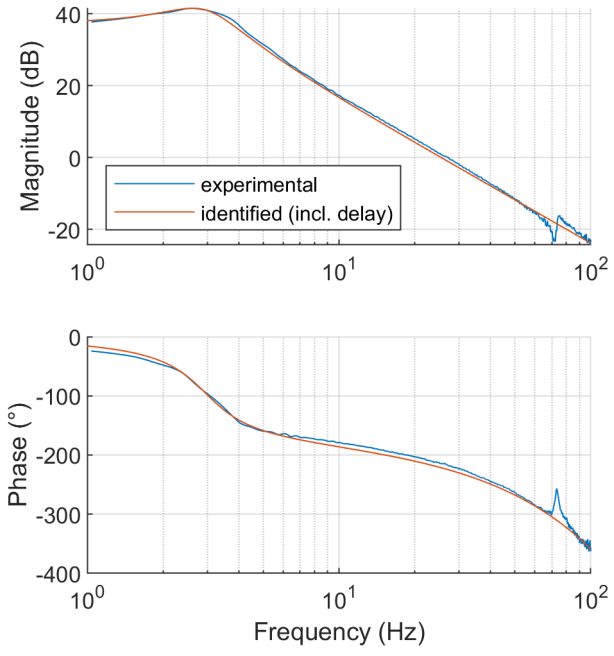

FIGURE 10. Bode plot of motor torque setpoint to measured spring torque (blue), and the identified second-order system approximation (red). The 5 ms delay is included in the identified system.

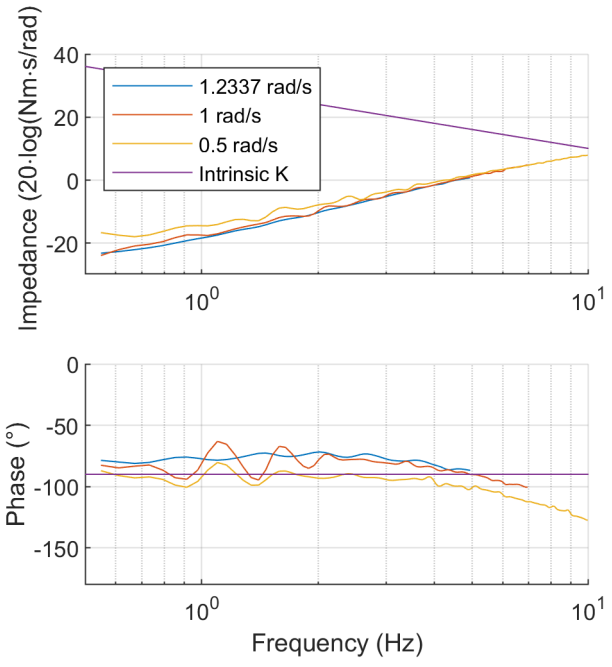

FIGURE 11. Output impedance measurements using various amplitudes of velocity chirp excitation. The purple line labeled "intrinsic K" is the impedance of an ideal 200 Nm/rad spring.

positioned to make the actuator axis coincide with the estimated hip flexion/extension axis. An indentation was added to the corset mesh above the iliac crest to prevent the corset from sliding down due to gravity. The hinge, just below the actuator, and the recirculating ball bearing rail on the thigh cuff make up the abduction/adduction mechanism. The rail was positioned parallel to the femur axis on the back of the thigh cuff. The lever arm connecting the actuator shaft to the thigh cuff was designed to fit the 3D model using the abovementioned software. The algorithmic nature of the

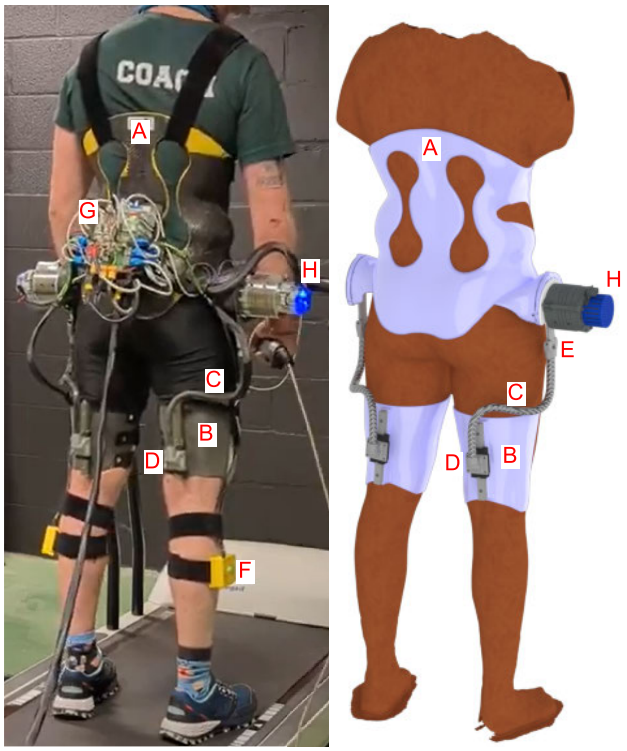

FIGURE 12. The trial participant wearing the exoskeleton (left) and a rendering of the 3D model (right). Components: corset (A), thigh cuffs (B), lever arms (C), rail (D), hinge (E), IMU (F), electronics (G), and actuator (H).

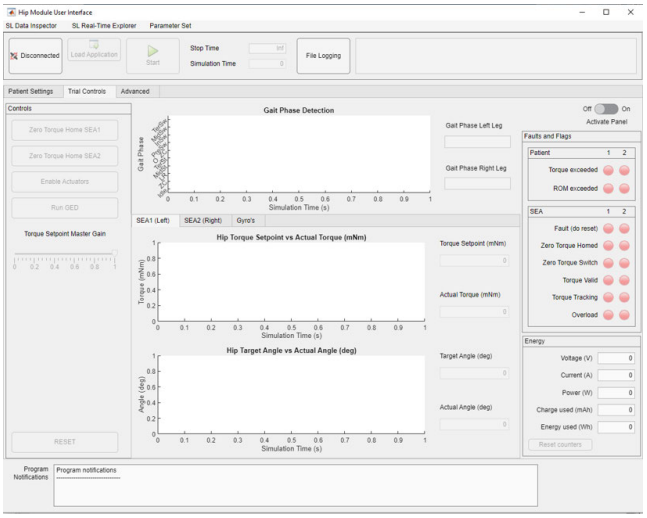

FIGURE 13. The main screen of the user interface, consisting of operator buttons (left), side-scrolling graphs of the gait phase detection, torque measurements, and angle measurements (center), and state indicators (right).

3D model makes it less labor-intensive to recreate similar orthotics for a new user.

The 3D model and the physical exoskeleton for our trial participant are shown in Fig. 12. The corset (Fig. 12, A) was manufactured using a fused deposition modeling (FDM) 3D printer with polylactic acid (PLA) material and reinforced with carbon fiber. The corset was closed in the front using velcro straps, and shoulder straps (NRX PLUS strap 30mm, Mediroyal Nordic AB, Sweden) were used for additional support. The thigh cuffs (Fig. 12, B) were made using a multi-jet fusion (MJF) 3D printer with polyamide 12 (PA12) material. The lever arm (Fig. 12, C) was made using MJF with PA12, reinforced with braided carbon fiber tubes, and glued to the connections using epoxy resin. The lever arm connections and hinge parts were made using laser powder bed fusion (PBF-LB/M) with AlSi10Mg material. The rail and carriage (Fig. 12, D) contain these components: rail HDR15 - 160L G:g=20:20, and carriage: HDR15CSS, THK Co., Ltd., Japan). The hinge (Fig. 12, E) includes iglidur P210 sleeve bearings, iglidur G thrust washers (Igus Gmbh, Germany), and a shoulder bolt machined to h7 tolerance to create a low backlash mechanism. The shank IMU cases (Fig. 12, F) were made using FDM with PLA and attached to the shank using neoprene rubber straps (NRX strap 30mm, Mediroyal Nordic AB, Sweden).

The range of motion (ROM) of the exoskeleton is 35° of extension, 95° of flexion, 16° of abduction, and 17° of adduction if the rail carriage is centered when the user is standing in the neutral position.

The combined mass of the worn part of the device is 8.6 kg. Each actuator weighs approximately 1.7 kg and the on-board electronics weigh 1 kg. The orthotics and other mechanical parts make up the remaining 4.2 kg.

F. EXOSKELETON CONTROL

The exoskeleton control consists of three parts: a gait event detection algorithm (GED) determines the current gait phase in real-time, followed by the execution of a corresponding assistive torque scheme, which determines the torque controller's setpoint. The GED algorithm is based on the gait phase detection (GPD) by Behboodi et al. [33], which was implemented in MATLAB and ported to Simulink Real-time for this hip exoskeleton. The algorithm uses the shank rotation in the sagittal plane, recorded by the gyroscopes in the two shank IMUs, and lowpass filtered to prevent false peak detection by using a second-order Butterworth filter with a cutoff frequency of 15 Hz. The IMUs and GED algorithm run at 100 Hz, whereas the lowpass filtering occurs at 1 kHz sample frequency. Several assistive torque schemes are conceivable, such as a constant torque or an impedance (virtual spring) mode, where the torque is calculated by multiplying a virtual spring constant with the difference between the measured output angle and a desired output angle. Only the constant torque mode was used in the human trial. The main screen of the user interface (Fig. 13) contains all the necessary buttons and indicators to operate the exoskeleton once the settings have been made on other screens.

The steps the operator must perform sequentially to run a trial are given in this list:

1) Don the exoskeleton while sitting on a stool or standing.

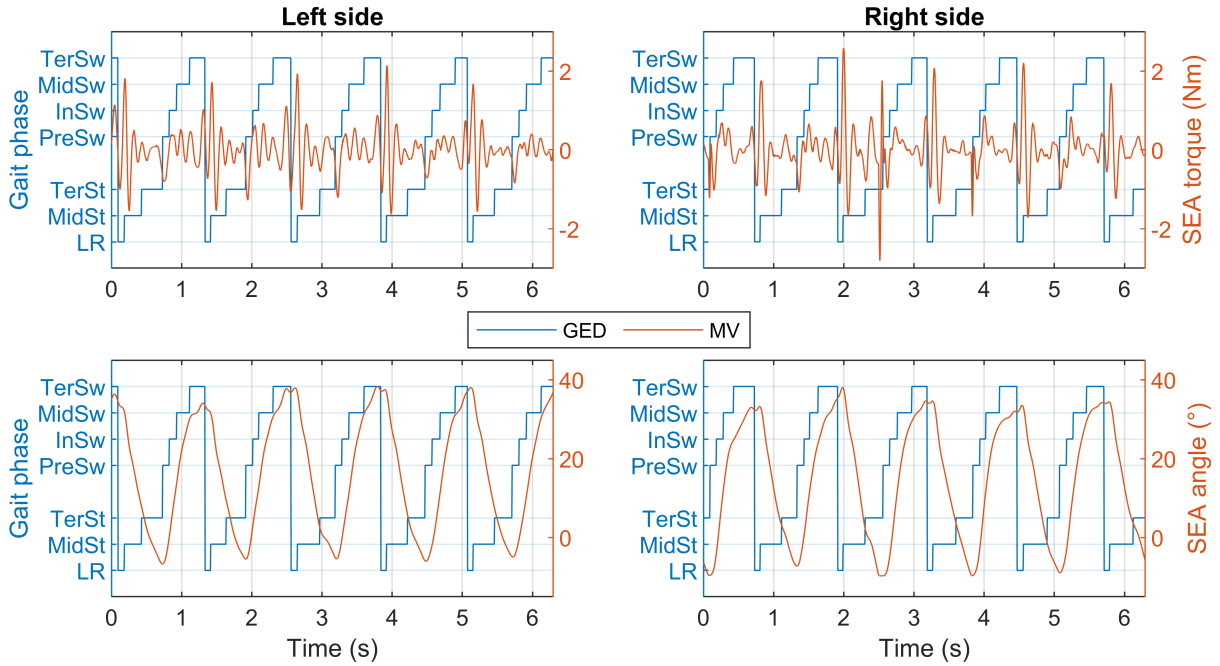

FIGURE 14. Experimental results of the human trial: five strides of normal walking in transparent mode. Legend explanation: GED = gait event detection, MV = measured value (torque and angle). The stance phases are loading response (LR), midstance (MidSt), terminal stance (TerSt), and preswing (PreSw). The swing phases are initial swing (InSw), midswing (MidSw), and terminal swing (TerSw).

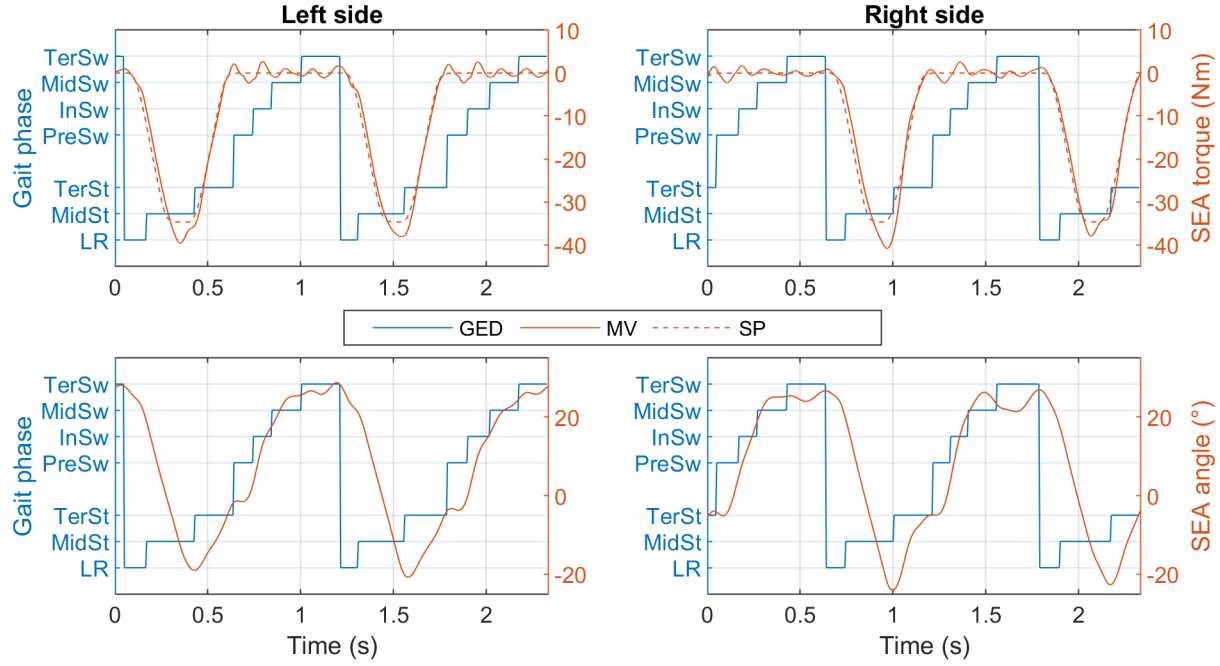

FIGURE 15. Experimental results of the human trial: two strides of normal walking, while 35 Nm of extension torque was commanded during loading response and midstance. Transparent mode was commanded during other gait phases. Legend explanation: GED = gait event detection, MV = measured value (torque and angle), SP = torque setpoint. The stance phases are loading response (LR), midstance (MidSt), terminal stance (TerSt), and preswing (PreSw). The swing phases are initial swing (InSw), midswing (MidSw), and terminal swing (TerSw).

2) Have the participant stand up and optionally insert a flexion mechanical stop.
3) Power up the exoskeleton and connect the computer. Run the user interface.
4) Enter or load participant-specific safety parameters and configure the torque assistance scheme.
5) Press the enabling switch, and then press "RESET". This clears the STO error.

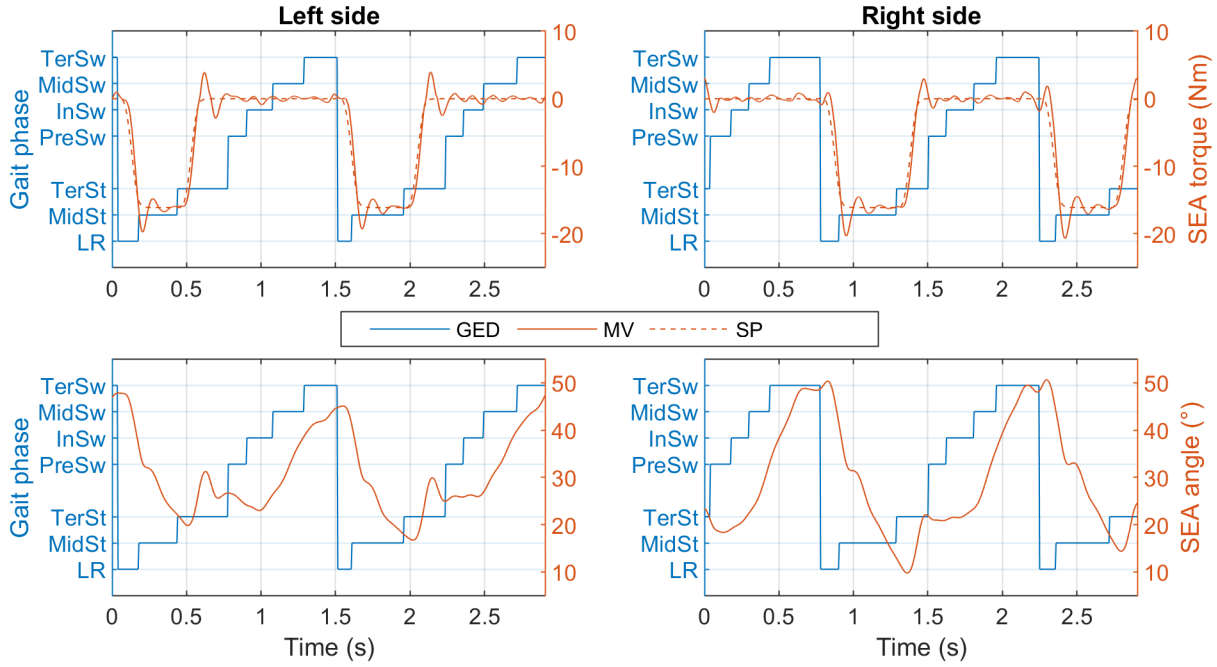

FIGURE 16. Experimental results of the human trial: two strides of simulated crouch gait, while 16 Nm of extension torque was commanded during loading response and midstance. Transparent mode was commanded during other gait phases. Legend explanation: GED = gait event detection, MV = measured value (torque and angle), SP = torque setpoint. The stance phases are loading response (LR), midstance (MidSt), terminal stance (TerSt), and preswing (PreSw). The swing phases are initial swing (InSw), midswing (MidSw), and terminal swing (TerSw).

6) Calibrate the actuators – press "Zero Torque Home" for both actuators while the needle triggers the optical switch (signaling the unloaded spring state) to home the incremental encoder of the motor.
7) Press "enable actuators". The exoskeleton should now track zero torque (transparent mode).
8) Let the patient initiate walking. Press "Run GED" to start GED.
9) Increasing the "Torque setpoint master gain" slider starts the assistance according to the scheme.
10) When the experiment is done, stop the user interface, power off, and doff the exoskeleton.

The following safety features were implemented, listed in ascending level of fault severity:

- If the actuator position is outside of safe angle bounds, then assistance is stopped (transparent mode) in the direction that would cause further exceeding of the limit. Torque in the opposite direction is still possible.
- If the actuator torque is outside of safe torque bounds, then the actuators are disabled through software but can be backdriven with ca. 10 Nm of torque.
- If the user or operator releases or hard-presses the enabling switch, then the actuators are disabled using the motor controller STO inputs but can be backdriven. This is a safety function using certified safety components.
- If the mechanical flexion(/extension) stop is reached, then no further flexion(/extension) travel is possible.

G. HUMAN TRIAL

Experiments were conducted on a healthy adult male participant who measured 174 cm tall and weighed 74.5 kg while walking on a treadmill. Informed consent was obtained. Initially, the exoskeleton was set to transparent mode, and the GED parameters were adjusted to ensure consistent detection. The performance of the transparent mode was evaluated by analyzing five steps taken at a walking speed of 4 km/h, as shown in Fig. 14. During this time, the rms and peak torque errors on the left side were 0.53 Nm and 2.1 Nm, respectively. On the right side, the errors were 0.57 Nm and 2.8 Nm, respectively. The largest error peaks coincide with the loading response. Next, the exoskeleton's torque-providing ability during stance was explored by incrementally increasing the setpoint until the controller became unstable due to motor saturation. A maximum torque setpoint of 35 Nm was achieved with a 1.2 s stride time without any instability issues, as depicted in Fig. 15. Finally, the participant was asked to imitate a crouched gait at 2 km/h while gradually increasing the extension torque during stance, as depicted in Fig. 16. With a setpoint of 16 Nm, he found it challenging to maintain a crouching pattern and reported a lifting sensation. A video of this experiment is included as the graphical abstract. There is a notable difference in actuator motion in Fig. 16, which may be attributable to the presence of more backlash and less stiffness in the mechanical human-exoskeleton interface on the right side. The SEA angle should not be confused with the angle of the hip joint itself.

III. DISCUSSION

Notable performance-critical aspects of the exoskeleton are discussed in this section.

To get the maximum performance out of an actuator featuring an electric motor, the current settings of the motor controller need to be set appropriately. The manufacturer's specifications are usually too conservative. For example, motor manufacturer maxon rates the current of their motors in a low-cooling scenario, where the stator is mounted to a bad thermal conductor, such as most plastics, and there is no forced convective cooling of the windings. In the case of our SEA, the motor is mounted to a large steel mass, the harmonic drive, that acts as a heatsink, and an always-on fan helps to cool the windings. This allowed the setting of a continuous current of 10 A instead of 7.25 A (138%). The short-burst current was set to 15 A, the maximum continuous current of the EPOS4 motor controller. This setting could be increased to 30 A, but this would overload the 20 A power supply, which would cause the internal overload protection to trip. The I^2t protection logic of the EPOS4 controller protects the motor windings from overheating during current bursts. If a lithium-polymer or a lithium-ion battery were used, a higher burst current setting would slightly improve performance.

The setpoint smoothing was implemented to mitigate undesired responses due to the 5 ms transport delay in the control loop. This effectively eliminated steps introduced to the controller by step-wise setpoint changes while incurring a performance penalty. However, sudden changes in control loop disturbance or system parameters when the leg transitions between stance and swing phase cannot be eliminated in this way, which can result in undesirable tracking errors. We recommend using high-speed, low-latency embedded hardware and software to run low-level torque controllers for SEAs. The transport delay should be measured if a communication bus, such as EtherCAT, is used in a feedback control loop.

The 3D model of the exoskeleton included sternum support, which had to be removed from the prototype to make it possible for the corset to be opened and donned. This caused discomfort at high extension torques due to pressure on the ribs. This feature should be redesigned in future iterations of the exoskeleton. The manufactured lever arm was slightly longer than the 3D model due to the carbon fiber tubes not seating fully into the connection parts, resulting in the carriage being lower on the rail when the participant stood in the neutral position. This meant that the abduction ROM was decreased, and the adduction ROM was increased.

IV. CONCLUSION

In summary, we presented a hip exoskeleton capable of providing gait-synchronized assistive flexion/extension torques while allowing hip abduction/adduction. We described the system architecture and the actuators' design concept. Furthermore, we identified the spring characteristic and an approximately equivalent second-order system of the actuators in the locked-output configuration. The controller architecture was presented based on a PD compensator, feedforward, and DOB. Relevant performance metrics were measured, such as bandwidth, overshoot, settling time, and output impedance. The controller proved stable and adequately tracked the torque setpoint, with the output connected to a pendulum that simulated the participant's leg's moment of inertia about the hip flexion/extension axis.

A prototype exoskeleton was built for an unimpaired participant, and its performance was evaluated during normal walking and simulated crouch gait. First, the control was set to transparent mode, and good tracking performance was achieved up to 4 km/h of walking speed, with rms and peak torque errors of 0.57 Nm and 2.8 Nm, respectively. Second, the limits of the exoskeleton to provide extension torque during stance was found to be 35 Nm. Finally, the participant simulated crouch gait while the extension torque setpoint was incrementally increased until he reported a lifting sensation at 16 Nm. This finding warrants further investigation. Future work should include testing the device on a patient with CP while measuring kinematics and kinetics using a motion capture system and hip flexor/extensor electromyography (EMG).

The exoskeleton could be improved by adding sternum support to the corset to increase comfort and torque transfer capacity further, and the performance of the torque control could be enhanced by using low-latency and high-speed electronics. Miniaturization of the electronics could also reduce the device's weight.

ACKNOWLEDGMENT

The authors would like to thank the following researchers and employees of the Mobilab&Care research group at Thomas More Kempen. Daniel R. Morales is credited for designing and building the orthotics and mechanical structure of the hip exoskeleton. Tom Saey provided Grasshopper code for locating anatomical landmarks on a 3D mesh and aligning parts to them. They also like to thank Koen Janssens for participating in the human trial and providing critical feedback on the exoskeleton's fitting, performance, and effects, and Roy Sevit for providing the MATLAB code for the gait event detection and for assisting with parameter tuning.

REFERENCES

[1] A. Nieuwenhuys, E. Papageorgiou, S.-H. Schless, T. De Laet, G. Molenaers, and K. Desloovere, "Prevalence of joint gait patterns defined by a Delphi consensus study is related to gross motor function, topographical classification, weakness, and spasticity, in children with cerebral palsy," *Frontiers Hum. Neurosci.*, vol. 11, p. 185, Apr. 2017.

[2] C. Cans, "Surveillance of cerebral palsy in Europe: A collaboration of cerebral palsy surveys and registers," *Develop. Med. Child Neurol.*, vol. 42, no. 12, pp. 816–824, Feb. 2007.

[3] E. Papageorgiou, A. Nieuwenhuys, I. Vandekerckhove, A. Van Campenhout, E. Ortibus, and K. Desloovere, "Systematic review on gait classifications in children with cerebral palsy: An update," *Gait Posture*, vol. 69, pp. 209–223, Mar. 2019.

[4] E. Beckung, G. Hagberg, P. Uldall, and C. Cans, "Probability of walking in children with cerebral palsy in Europe," *Pediatrics*, vol. 121, no. 1, pp. e187–e192, Jan. 2008.

[5] D. R. Patel, M. Neelakantan, K. Pandher, and J. Merrick, "Cerebral palsy in children: A clinical overview," *Transl. Pediatrics*, vol. 9, no. S1, pp. S125–S135, Feb. 2020.

[6] R. Palisano, P. Rosenbaum, S. Walter, D. Russell, E. Wood, and B. Galuppi, "Development and reliability of a system to classify gross motor function in children with cerebral palsy," *Develop. Med. Child Neurol.*, vol. 39, no. 4, pp. 214–223, Sep. 2008.

[7] M. Matsuda, Y. Mataki, H. Mutsuzaki, K. Yoshikawa, K. Takahashi, K. Enomoto, K. Sano, M. Mizukami, K. Tomita, H. Ohguro, and N. Iwasaki, "Immediate effects of a single session of robot-assisted gait training using hybrid assistive limb (HAL) for cerebral palsy," *J. Phys. Therapy Sci.*, vol. 30, no. 2, pp. 207–212, 2018.

[8] M. Matsuda, N. Iwasaki, Y. Mataki, H. Mutsuzaki, K. Yoshikawa, K. Takahashi, K. Enomoto, K. Sano, A. Kubota, T. Nakayama, J. Nakayama, H. Ohguro, M. Mizukami, and K. Tomita, "Robot-assisted training using hybrid assistive Limb for cerebral palsy," *Brain Develop.*, vol. 40, no. 8, pp. 642–648, Sep. 2018.

[9] S. Nakagawa, H. Mutsuzaki, Y. Mataki, Y. Endo, M. Matsuda, K. Yoshikawa, H. Kamada, and M. Yamazaki, "Newly developed hybrid assistive limb for pediatric patients with cerebral palsy: A case report," *J. Phys. Therapy Sci.*, vol. 31, no. 8, pp. 702–707, 2019.

[10] S. Nakagawa, H. Mutsuzaki, Y. Mataki, Y. Endo, M. Matsuda, K. Yoshikawa, H. Kamada, N. Iwasaki, and M. Yamazaki, "Safety and immediate effects of hybrid assistive limb in children with cerebral palsy: A pilot study," *Brain Develop.*, vol. 42, no. 2, pp. 140–147, Feb. 2020.

[11] Y. He, D. Eguren, T. P. Luu, and J. L. Contreras-Vidal, "Risk management and regulations for lower limb medical exoskeletons: A review," *Med. Devices: Evidence Res.*, vol. 10, pp. 89–107, May 2017.

[12] M. Bionics. (2023). *Atlas Pediatric Exo Product Detail*. Accessed: Jul. 4, 2023. [Online]. Available: https://www.marsibionics.com/en/atlas-pediatric-exo-product-detail/

[13] M. Cestari, D. Sanz-Merodio, and E. Garcia, "Preliminary assessment of a compliant gait exoskeleton," *Soft Robot.*, vol. 4, no. 2, pp. 135–146, Jun. 2017.

[14] K. A. Shorter, J. Xia, E. T. Hsiao-Wecksler, W. K. Durfee, and G. F. Kogler, "Technologies for powered ankle-foot orthotic systems: Possibilities and challenges," *IEEE/ASME Trans. Mechatronics*, vol. 18, no. 1, pp. 337–347, Feb. 2013.

[15] G. M. Gasparri, M. O. Bair, R. P. Libby, and Z. F. Lerner, "Verification of a robotic ankle exoskeleton control scheme for gait assistance in individuals with cerebral palsy," in *Proc. IEEE/RSJ Int. Conf. Intell. Robots Syst. (IROS)*, Oct. 2018, pp. 4673–4678.

[16] Z. F. Lerner, D. L. Damiano, H.-S. Park, A. J. Gravunder, and T. C. Bulea, "A robotic exoskeleton for treatment of crouch gait in children with cerebral palsy: Design and initial application," *IEEE Trans. Neural Syst. Rehabil. Eng.*, vol. 25, no. 6, pp. 650–659, Jun. 2017.

[17] S. S. P. A. Bishe, L. Liebelt, Y. Fang, and Z. F. Lerner, "A low-profile hip exoskeleton for pathological gait assistance: Design and pilot testing," in *Proc. Int. Conf. Robot. Autom. (ICRA)*, May 2022, pp. 5461–5466.

[18] F. Giovacchini, F. Vannetti, M. Fantozzi, M. Cempini, M. Cortese, A. Parri, T. Yan, D. Lefeber, and N. Vitiello, "A light-weight active orthosis for hip movement assistance," *Robot. Auto. Syst.*, vol. 73, pp. 123–134, Nov. 2015.

[19] K. Langlois, M. Moltedo, T. Bacek, C. Rodriguez-Guerrero, B. Vanderborght, and D. Lefeber, "Design and development of customized physical interfaces to reduce relative motion between the user and a powered ankle foot exoskeleton," in *Proc. 7th IEEE Int. Conf. Biomed. Robot. Biomechatronics (Biorob)*, Aug. 2018, pp. 1083–1088.

[20] I. Kang, H. Hsu, and A. Young, "The effect of hip assistance levels on human energetic cost using robotic hip exoskeletons," *IEEE Robot. Autom. Lett.*, vol. 4, no. 2, pp. 430–437, Apr. 2019.

[21] J. Chen, Y. Dai, N. S. Grimaldi, J. Lin, B. Hu, Y. Wu, and S. Gao, "Plantar pressure-based insole gait monitoring techniques for diseases monitoring and analysis: A review," *Adv. Mater. Technol.*, vol. 7, no. 1, Jan. 2022, Art. no. 2100566, doi: 10.1002/admt.202100566.

[22] M. D. C. Sanchez-Villamañan, J. Gonzalez-Vargas, D. Torricelli, J. C. Moreno, and J. L. Pons, "Compliant lower limb exoskeletons: A comprehensive review on mechanical design principles," *J. NeuroEng. Rehabil.*, vol. 16, no. 1, p. 55, Dec. 2019.

[23] S. De Groof, Y. Zhang, L. Peyrodie, R. Sevit, E. Vander Poorten, E. Aertbelien, and L. Labey, "Design of a series elastic actuator for an assistive exoskeleton using numerical methods and gait data," in *Proc. ACTUATOR Int. Conf. Exhib. New Actuator Syst. Appl.*, Jun. 2022, pp. 1–4.

[24] H. J. van de Straete, P. Degezelle, J. De Schutter, and R. J. M. Belmans, "Servo motor selection criterion for mechatronic applications," *IEEE/ASME Trans. Mechatronics*, vol. 3, no. 1, pp. 43–50, Mar. 1998.

[25] J. Vantilt, "Development of a model-based controller for a bilateral lower-limb exoskeleton with series elastic actuators," Ph.D. dissertation, Arenberg Doctoral School, Fac. Eng. Sci., KU Leuven, Leuven, Belgium, 2018.

[26] B. Ugurlu, E. Sariyildiz, A. T. Kansizoglu, E. C. Ozcinar, and S. Coruk, "Benchmarking torque control strategies for a torsion-based series elastic actuator," *IEEE Robot. Autom. Mag.*, vol. 29, no. 2, pp. 85–96, Jun. 2022.

[27] E. Sariyildiz, R. Oboe, and K. Ohnishi, "Disturbance observer-based robust control and its applications: 35th anniversary overview," *IEEE Trans. Ind. Electron.*, vol. 67, no. 3, pp. 2042–2053, Mar. 2020.

[28] N. Paine, S. Oh, and L. Sentis, "Design and control considerations for high-performance series elastic actuators," *IEEE/ASME Trans. Mechatronics*, vol. 19, no. 3, pp. 1080–1091, Jun. 2014.

[29] N. Paine, J. S. Mehling, J. Holley, N. A. Radford, G. Johnson, C.-L. Fok, and L. Sentis, "Actuator control for the NASA-JSC Valkyrie humanoid robot: A decoupled dynamics approach for torque control of series elastic robots: Actuator control for the NASA-JSC valkyrie humanoid robot," *J. Field Robot.*, vol. 32, no. 3, pp. 378–396, May 2015.

[30] Y. Lin, Z. Chen, and B. Yao, "Decoupled torque control of series elastic actuator with adaptive robust compensation of time-varying load-side dynamics," *IEEE Trans. Ind. Electron.*, vol. 67, no. 7, pp. 5604–5614, Jul. 2020.

[31] T.-I. Kim, J.-S. Han, T.-H. Oh, Y.-S. Kim, S.-H. Lee, and D.-I. 'Dan' Cho, "A new accurate discretization method for high-frequency component mechatronics systems," *Mechatronics*, vol. 62, Oct. 2019, Art. no. 102250.

[32] K. J. Astrom and B. Wittenmark, *Computer-Controlled Systems: Theory and Design* (Prentice-Hall Information and System Sciences Series), 3rd ed. Upper Saddle River, NJ, USA: Prentice-Hall, 1997.

[33] A. Behboodi, N. Zahradka, H. Wright, J. Alesi, and S. C. K. Lee, "Real-time detection of seven phases of gait in children with cerebral palsy using two gyroscopes," *Sensors*, vol. 19, no. 11, p. 2517, Jun. 2019.

SANDER DE GROOF received the B.S. and M.S. degrees in electromechanical engineering technology from KU Leuven, in 2014 and 2015, respectively, where he is currently pursuing the Ph.D. degree in engineering technology.

From 2015 and 2019, he was an Electrical Engineer and a Software Engineer in the industrial automation sector. He is currently developing a hip flexion and extension exoskeleton containing custom-built series elastic actuators. His research interests include robotic assistive devices, actuator modeling, mechanical design, and (real-time) control.

YANG ZHANG was born in Karamay, Xinjiang, China, in 1990. He received the B.S. degree in aircraft design and engineering and the M.S. degree in solid mechanics from Northwestern Polytechnic University, Xi'an, China, in 2012 and 2015, respectively, and the Ph.D. degree in mechanical engineering from Institut national des sciences appliquées de Rennes, France, in 2019.

From 2019 and 2022, he was a Postdoctoral Researcher and a Contractual Lecture with the Department of Smart System and Energy, HEI-JUNIA, Lille. Since 2022, he has been a Research Engineer with Flanders Make, Belgium. His research interests include robotic assistive devices for rehabilitation, mechanism design, intelligent industrial robotic systems, and gravity balancing for robots.

LAURENT PEYRODIE was born in Tourcoing, France, in 1968. He received the Ph.D. degree in automation, production, and industrial computing and the Habilitation degree from the University of Lille 1, France, in 1996 and 2010, respectively.

From 1999 to 2010, he was an Assistant Professor with Hautes Études d'Ingénieur Lille. Since 2010, he has been an Associate Professor with HEI-JUNIA, Lille. He is a Specialist in signal/image processing and biomedical signals. He is the Team Leader of the ''Robotic-Mechanic'' Team, HEI-JUNIA, and the Leader of two European Interreg projects. He has published more than 60 papers in international journals and conferences. His research interests include biomedical processing, EEG signals, particularly in EEG signal filtering, and epilepsy seizure detection.

LUC LABEY received the degree in materials engineering and the Ph.D. degree with a focus on biomechanics of the knee joint and knee implants from KU Leuven, in 1988 and 2003, respectively. After the Ph.D. with KU Leuven, he was the Lead Project Manager of the Smith and Nephew's European Centre for Knee Research, Leuven, Belgium, from 2006 to 2013. Since 2013, he has been an Associate Professor with KU Leuven. He specializes in biomechanics, biomaterials, and orthopaedic technology. He is currently a Coordinator of the Research and Education-Electromechanics-Energy and a contact person of BioMechanics (BMe), KU Leuven Campus Geel. He has published more than 150 papers in international journals and conferences. His research interest includes biomechanical engineering of medical devices.